



# Experimental determination of the lidar ratio for cirrus and polar stratospheric clouds at Dome C, Antarctica, using a Young inversion

Francesco Cairo<sup>1</sup>, Luca Di Liberto<sup>1</sup>, Alessandro Bracci<sup>1</sup>, and Marcel Snels<sup>1</sup>

<sup>1</sup>Institute of Atmospheric Sciences and Climate (ISAC), National Research Council (CNR), Italy

**Correspondence:** Francesco Cairo (francesco.cairo@cnr.it)

## Abstract.

We present three years (2022–2024) of polarisation lidar observations of polar stratospheric clouds (PSCs) and tropospheric cirrus above Concordia Station (Dome C, Antarctica). Layer-mean lidar ratios (LR) at 532 nm are retrieved using the Young inversion method applied to an elastic backscatter and depolarisation (Rayleigh) lidar. The measurements are classified in the  $(1 - 1/R, \delta_T)$  phase space, allowing us to separate supercooled ternary solution (STS), nitric-acid trihydrate (NAT) and ice PSC, as well as upper-tropospheric cirrus.

To quantify the impact of the Young assumptions, we analyse both the full set of cloud detections and a Young-optimized subset of clouds that satisfy stricter homogeneity conditions above and below the cloud layer. The comparison between these two datasets allows us to separate the effective climatological variability of lidar ratio values from those retrieved under idealised conditions that strictly satisfy the Young inversion assumptions. For PSCs, the full dataset yields optically weighted median LR values (25–75 percentiles) of 38 (31–52) sr for STS, 50 (37–73) sr for NAT, and 52 (40–65) sr for ice PSC. For cirrus, the median LR is 49 (34–52) sr. These values are consistent with microphysical expectations and with previous ground-based and spaceborne lidar studies.

The Young-optimized subset yields 41 (31–61) sr for STS, 61 (38–78) sr for NAT, 38 (32–38) sr for the few remaining ice PSC, and 41 (31–41) sr for cirrus although for this latter case the number of observations is not statistically significant. The subset thus provides a conservative estimate of the accuracy of the results from the full dataset which can capture the full range of cloud variability.

These values provide a physically consistent reference for PSC and cirrus retrievals over Dome C and can be used in radiative-transfer modelling and satellite-lidar validation.

20

## 1 Introduction

Cirrus clouds in the troposphere and polar stratospheric clouds (PSCs) in Antarctica play a central role in the radiative budget, transport and dehydration processes, and, in the case of PSCs, the heterogeneous chemistry responsible for polar ozone deple-



tion (Solomon, 1999; Peter and Groö, 2012). Polarization diversity Rayleigh lidars provide continuous vertical profiling of  
25 cloud backscatter and depolarization, allowing discrimination between ice, supercooled ternary solutions (STS), and nitric acid  
trihydrate (NAT) particles (Pitts et al., 2018; Hostetler et al., 2006). A key parameter controlling the conversion of attenuated  
backscatter into extinction is the lidar ratio (LR), which directly links the optical and microphysical properties of cloud parti-  
cles. Accurate LR values are essential for retrieving cloud optical depth, quantifying radiative effects, and constraining particle  
phase and habit (Reichardt et al., 2004; Ansmann et al., 1992).

30 Ground-based and satellite Rayleigh lidar measurements do not provide independent constraints on backscattering and ex-  
tinction simultaneously; consequently, such studies have often relied on fixed or aerosol- and cloud-type-dependent LR values.  
For PSCs, early modelling analyses suggested LR in the range 40–70 sr, with lower values associated with liquid/STS lay-  
ers and higher values for NAT- and ice-dominated clouds (Gobbi, 1995). In practice, several long-term PSC data sets have  
adopted constant LR of 40–50 sr for all PSC types or for specific categories: for example, Córdoba-Jabonero et al. (2013) used  
35  $S = 40$  sr in Arctic micropulse-lidar observations, while CALIPSO operational products assume fixed LR of order 50 sr for all  
PSC classes (Kim et al., 2018), while refined PSC-type based choices have also been implemented (Pitts et al., 2018). More  
recent case studies exploiting Raman or Rotational–Raman channels have started to retrieve LR directly, reporting values of  
 $LR_{355} = 20–25$  sr and  $LR_{532} = 55–60$  sr for spherical PSC observed over the European Arctic (Böckmann and Ritter, 2023),  
and confirming that ice and NAT PSC can reach LR well above 60 sr in mountain-wave events (Reichardt et al., 2004). Noel  
40 et al. (2009) reported low to medium values lidar ratios LR=20–50 sr are consistent with type II PSC.

A further complication is that background stratospheric aerosol itself can have LR comparable to that of PSC. Raman-lidar  
measurements at Antarctic and Arctic sites indicate LR of  $\sim 50–60$  sr at 532 nm for volcanically enhanced sulfate aerosol  
(David et al., 2012; Achtert et al., 2013).

For cirrus, a similarly broad range of lidar ratio values has been reported. Ground-based and spaceborne retrieval algorithms  
45 often assume fixed LR values of 25–30 sr (Josset et al., 2012; Kim et al., 2018), while direct measurements show site-dependent  
mean values ranging from  $\sim 30$  sr at mid-latitudes (Chen et al., 2002; Holz et al., 2002; Yorks et al., 2011) up to  $\sim 40–45$  sr in  
polar regions, with median cirrus LR of  $42 \pm 10$  sr reported over Nyålesund (Nakoudi et al., 2021). Long-term lidar observations  
have further shown that such variability in cirrus optical properties has direct implications for radiative forcing estimates, with  
constrained lidar-ratio ranges commonly adopted to ensure physically consistent extinction retrievals (Lolli et al., 2025).

50 This spread reflects changes in particle shape, size and habit related to temperature, ventilation and water vapour availability,  
and, in the case of PSC, temperature-dependent transitions between STS, NAT and ice (Luo et al., 2003; Höpfner et al., 2006).

Such variability introduces uncertainty in extinction corrections and hence in the interpretation of PSC and cirrus optical,  
microphysical and radiative properties when a single lidar ratio value is assumed to be representative of all cloud conditions.  
This uncertainty is further enhanced in mixed-phase polar stratospheric clouds, where the coexistence of STS, NAT and ice  
55 particles with different shapes and size distributions leads to complex and non-linear optical scattering behaviour (Cairo et al.,  
2023). A physically based alternative is the Young inversion method (Young, 1995; Young and Vaughan, 2009), which retrieves  
LR by enforcing cloud top–bottom consistency of the backscatter ratio after extinction correction. While this approach is  
routinely used in CALIPSO/CALIOP processing (Vaughan et al., 2004; Kim et al., 2018), long-term applications to ground-



based polar lidar observations remain relatively limited, and the range of LR values obtained under strictly controlled Young  
60 conditions has not yet been fully characterised for PSCs and cirrus at Dome C.

Dome C (Concordia Station, 75°06'S, 123°23'E) provides a unique setting for cloud research. Extremely low winter tem-  
peratures, stable meteorological conditions, and the long polar night enable uninterrupted observation of PSCs and upper-  
tropospheric cirrus. Previous studies have documented PSC occurrence and optical properties at Dome C (Snels et al., 2021;  
65 Di Liberto et al., 2024), highlighting the site's potential for long-term monitoring and microphysical characterization. However,  
a systematic determination of LR for all major PSC types and cirrus using a uniform inversion method has not yet been carried  
out.

In this work we present a comprehensive determination of the lidar ratio for cirrus and for all PSC classes observed at Dome C  
using an implementation of the Young inversion applied to multi-year (2022–2024) 532 nm polarization lidar profiles. The  
processing chain includes crosstalk correction, molecular and aerosol extinction removal, cloud detection, and iterative cloud  
70 LR retrieval. A dedicated statistical module aggregates all retrieved cloud points and produces optically weighted distributions  
in backscatter–depolarization space, enabling the robust separation of STS, NAT, ice PSCs and cirrus. In this framework, the  
distinction between PSCs and cirrus clouds is performed using the altitude of the climatological tropopause as a reference: cloud  
points above this level are classified as PSCs, whereas those below are identified as cirrus. The resulting dataset represents the  
first unified ground-based LR climatology for polar clouds at Dome C, providing new observational constraints for lidar data  
75 processing, cloud radiative studies and for the evaluation of microphysical and chemical models in Antarctic conditions.

From a methodological perspective, this study explicitly distinguishes between lidar-ratio statistics derived from the full  
population of detected cloud layers and those obtained from a subset satisfying stricter Young homogeneity conditions. The  
former captures the full microphysical and dynamical variability of polar clouds, while the latter provides a physically con-  
servative benchmark representative of vertically uniform layers for which the Young inversion assumptions are most closely  
80 fulfilled.

## 2 Site and instrumentation

### 2.1 Concordia Station (Dome C)

The observations analysed in this study were collected at Concordia Station (Dome C, 75°06'S, 123°23'E; 3233 m a.s.l.) on  
the East Antarctic plateau. The site is characterized by extremely low temperatures, particularly during the austral winter, with  
85 frequent occurrence of PSCs between June and September. The high altitude and the radiative cooling of the ice sheet strongly  
reduce tropospheric aerosol loadings, providing exceptionally clean background conditions for polarization lidar measure-  
ments. These conditions, combined with the long polar night, enable continuous operation of the instrument and extended time  
series suitable for cloud optical characterisation (Snels et al., 2021; Di Liberto et al., 2024). Over the June–October period, the  
dataset used here comprises 144 measurement days in 2022, 90 in 2023, and 112 in 2024. The lidar system used in this work  
90 is a ground-based, single-wavelength, polarization-sensitive lidar operating at 532 nm. The lidar transmitter emits linearly po-  
larised pulses at a repetition rate of 10 Hz. The receiver unit includes a Schmidt–Cassegrain telescope coupled to a two-channel



polarization separation module, detecting the parallel and cross-polarized components ( $P_{\parallel}$  and  $P_{\perp}$ ) of the backscattered light. The effective vertical resolution of the processed profiles is 30–60 m, depending on the acquisition configuration, and the temporal integration is 2 minutes, or 32 minutes when 16 recordings are averaged, which is the normal procedure.

95 Raw signals are stored as photon-counting profiles, together with auxiliary molecular backscatter coefficients  $\beta_{\text{mol}}$  computed from co-located radiosonde measurements or standard atmospheric models. The lidar is routinely used for the detection and classification of cirrus clouds and PSCs at Dome C, and has been employed in previous coordinated studies with CALIPSO/CALIOP validations (Snels et al., 2021).

From the height-resolved measurements of parallel and cross-polarized backscatter signals, the volume backscatter coefficients  $\beta_{\parallel}(z)$  and  $\beta_{\perp}(z)$  can be retrieved, which contain contributions from both molecules and particles. Hence, volume depolarization ratios, and backscatter ratios, can be assessed. The volume depolarization ratio  $\delta$  is defined as

$$\delta(z) = \frac{\beta_{\perp}(z)}{\beta_{\parallel}(z)} = \frac{\beta_{\perp}^{\text{mol}}(z) + \beta_{\perp}^{\text{aer}}(z)}{\beta_{\parallel}^{\text{mol}}(z) + \beta_{\parallel}^{\text{aer}}(z)}.$$

The backscatter ratio is

$$R(z) = \frac{\beta_{\parallel}(z) + \beta_{\perp}(z)}{\beta_{\parallel}^{\text{mol}}(z) + \beta_{\perp}^{\text{mol}}(z)} = 1 + \frac{\beta_{\text{aer}}(z)}{\beta_{\text{mol}}(z)},$$

105 where

$$\beta_{\text{aer}} = \beta_{\parallel}^{\text{aer}} + \beta_{\perp}^{\text{aer}}, \quad \beta_{\text{mol}} = \beta_{\parallel}^{\text{mol}} + \beta_{\perp}^{\text{mol}}.$$

The aerosol (particle) and molecular depolarization ratios are defined as:

$$\delta_{\text{A}}(z) = \frac{\beta_{\perp}^{\text{aer}}(z)}{\beta_{\parallel}^{\text{aer}}(z)}, \quad \delta_{\text{mol}} = \frac{\beta_{\perp}^{\text{mol}}(z)}{\beta_{\parallel}^{\text{mol}}(z)}.$$

Following Adachi et al. (2001) and Gimmestad (2008), we analyse the measurements in terms of the Total Particle Depolarization Ratio ( $\delta_{TA}$ ) and the Total Depolarization Ratio ( $\delta_T$ ). Gimmestad (2008) showed that adopting the  $\delta_T$  definition provides a more coherent framework that harmonizes lidar depolarization analysis with radiative transfer theory, particle-scattering theory, and standard polarization measurement techniques.

The total volume depolarization ratio (Cairo et al., 1999) is

$$\delta_T(z) = \frac{\beta_{\perp}(z)}{\beta_{\perp}(z) + \beta_{\parallel}(z)} = \frac{\delta(z)}{\delta(z) + 1}.$$

115 Similarly, the total particle depolarization is

$$\delta_{TA}(z) = \frac{\beta_{\perp}^{\text{aer}}(z)}{\beta_{\parallel}^{\text{aer}}(z)} = \frac{\delta_{\text{mol}} + (R(z) - 1) \delta_{\text{A}}(z)}{R(z)}.$$

These quantities enable the retrieval of aerosol and cloud backscatter and the identification of microphysical regimes (STS, NAT, ice PSCs, cirrus) through combined analysis of backscatter enhancement and depolarization signatures. The subsequent processing described in Sect. 3 and Sect. 4 explains how these these primary observations are retrieved



### 120 3 Data processing and methodology

The raw lidar data consist of photon-counting profiles from the parallel ( $P_{\parallel}$ ) and cross-polarized ( $P_{\perp}$ ) channels acquired simultaneously by two partially overlapping acquisition chains at 60 m vertical resolution, a high-dynamic-range “tropospheric” channel and a more sensitive “stratospheric” channel each with its own telescope. Prior to inversion, the two channels are merged into a single continuous profile and processed through a sequence of calibration, crosstalk correction, molecular and aerosol extinction removal, cloud detection, and Young-type lidar ratio retrieval, as described below.

Dark counts are obtained from the uppermost part of the profile and subtracted from the raw photon counts. Profiles are optionally smoothed with a short moving-average filter over a 300 m window to suppress noise while preserving cloud boundaries. Statistical uncertainties are computed assuming Poisson statistics and uncertainty profiles are smoothed and stored as part of the final data product. The tropospheric channel provides a better linearity at low levels at the expense of a reduced signal-to-noise ratio, whereas the stratospheric channel ensures higher sensitivity in the upper atmosphere. The two channels are first background subtracted and range-corrected and normalized to their respective dynamic ranges. An altitude-dependent weighting function produces a smooth transition between the two, ensuring continuity in the overlap region. A final consistency check compares the mean molecular signals in the overlap range. The resulting merged profiles serve as the base input for all subsequent steps.

Auxiliary molecular backscatter coefficients  $\beta_{\text{mol}}(z)$  are computed from co-located radiosonde measurements and, when unavailable, from standard atmospheric models. These are used to calculate the attenuated total backscatter and the corresponding attenuated backscatter ratio  $R_{\text{att}}$ . In addition, the ratio  $D$  of the cross- to parallel-channel signals ( $P_{\perp}/P_{\parallel}$ ), proportional to the volume depolarization, is examined to identify altitude regions free of aerosol together with  $R_{\text{att}}$ .

A calibration interval is required to normalize the backscatter ratio and depolarization to their molecular reference values. A two-step automatic search scans the profile for candidate molecular regions where  $R_{\text{att}} \lesssim 1$  and  $D \approx \delta_{\text{mol}}$ . Among these candidates, the segment minimizing the variance of both quantities is selected as the calibration interval. If no sufficiently stable region is found, a fixed calibration range is retrieved from a precompiled lookup table. This approach ensures robust and repeatable normalization across the multi-year dataset.

Accurate polarization measurements require correction for optical and electronic crosstalk (CT) and for the gain ratio  $G \approx g_{\parallel}/g_{\perp}$  of the detection channels, where  $P_{\parallel,\perp} \sim g_{\parallel,\perp}\beta_{\parallel,\perp}$ . Following the molecular-consistency approach originally proposed in Di Liberto et al. (2024), the calibration relies on the fact that in purely molecular layers the ratio of the gain- normalized and cross-talk corrected cross-polarised to the parallel backscatter must equal the known molecular depolarisation  $\delta_{\text{mol}}$  which in our case, given the characteristics of the lidar, should attain the value 0.007 (Behrendt and Nakamura, 2002)

In principle, both  $G$  and CT can be obtained through independent laboratory or on-site calibration procedures. When these measurements remain stable, the molecular-consistency requirement acts purely as a diagnostic check: any residual particulate depolarisation retrieved in the molecular reference region indicates imperfect calibration.

In practice, however, both parameters may undergo slow drifts due to detector ageing, thermal effects or optical realignment or change in the optical channels transmission and cross contamination. Because these drifts do not necessarily affect  $G$  and



CT on the same timescale, it is often the case that one parameter (typically  $G$ ) remains better constrained than the other. The  
155 inversion framework therefore offers a second operating mode: the more reliable parameter can be fixed, and the remaining  
one is adjusted so as to satisfy the molecular-consistency condition. This procedure does not “force” the cloud retrievals, but  
instead ensures that the instrument remains self-consistent in conditions where the true molecular depolarisation is known a  
priori.

After applying the selected correction scheme, the parallel and cross-polar signals are renormalised to obtain crosstalk-free  
160 profiles of attenuated backscatter ratio  $R_{att}$  and depolarisation  $\delta$ , which form the basis for the subsequent Young inversion.  
The attenuated backscatter ratio is corrected for Rayleigh extinction using a molecular lidar ratio of 8.4 sr.

To perform the Young inversion, the cloud boundaries must be accurately identified, since the method requires a well-defined  
interval over which the extinction correction is applied. However, the presence of cloud extinction itself deforms the attenu-  
ated backscatter ratio making the direct detection of cloud top and base less reliable. For this reason, an intermediate step is  
165 introduced.

First, a provisional cloud extinction correction is applied by assuming a fixed lidar ratio of 30 sr. This choice is not meant to  
reflect the true cloud optical properties, but simply to reduce the attenuation-induced curvature of  $R_{att}$  and thereby make the  
cloud-edge gradients more pronounced. Cloud boundaries are then detected on this provisionally corrected profile.

The procedure is iterative: the boundaries obtained after the first pass are used to refine the provisional extinction correction,  
170 which further improves the localisation of the cloud edges, and the process is repeated until the cloud interval converges.  
Clouds are identified as contiguous altitude intervals where  $R_{fixed} > 1.15$  and the thickness exceeds a fixed altitude interval.  
Multiple fragments separated by fewer than 300 m are merged. The resulting cloud intervals form the altitude regions where to  
apply the Young inversion. Once the cloud top and base are robustly determined, the provisional correction is discarded, and  
the Young inversion is applied to the original, uncorrected attenuated backscatter profile. Then, a second correction removes  
175 background aerosol extinction using a fixed aerosol LR of 70 sr in regions of the profile where no clouds are present, as inside  
cloud layers the LR will be retrieved via the Young inversion.

The optimal cloud LR is obtained by selecting the value that minimises the absolute difference between the mean corrected  
backscatter ratio  $R_{cor}$  computed in two 240 m windows located 180 m above and below the cloud boundaries. At each trial  
value of the LR, an internal short iteration is performed:  $R$  is updated inside the cloud, the extinction correction is recomputed,  
180 and the top-bottom consistency is evaluated again. The process converges rapidly, yielding the LR that best satisfies the Young  
condition.

### 3.1 Selection of clouds best suitable for unbiased Young inversion

The lidar ratio retrieved by the Young inversion relies on the assumption that the backscatter ratio  $R$  is identical immediately  
above and below an homogeneous cloud layer (Del Guasta, 1998; Iwabuchi et al., 2002). In real atmospheric conditions this  
185 requirement may be violated, especially for clouds exhibiting strong vertical gradients, embedded sub-layers, mixed-phase  
transitions or residual background aerosol. For this reason, we analyse the lidar ratio using two complementary approaches:  
(i) the full measurement set, providing the broadest and most complete representation of the observed variability, and (ii)



a Young–optimised subset of clouds that satisfy stringent conditions and for which the inversion could be more physically robust.

190 The rationale for including the full data set is that biases introduced by local violations of the Young assumptions might be randomly distributed across the LR domain and, therefore, might not significantly affect the central tendency of the LR distribution. Under this working hypothesis, the mean or median LR computed over the entire population would still yield a realistic representation of the climatological LR range for each cloud category, even if individual retrievals were affected by local errors. This approach preserves the full diversity of cloud structures observed above Dome C, including mesoscale  
195 temperature variation inducing ice PSCs, NAT/ice transitions, and multi-layer cirrus.

To obtain a complementary set of likely unbiased retrievals we constructed a Young–optimised subset by applying a sequence of more stringent homogeneity criteria designed to isolate clouds embedded in quasi-molecular conditions above and below. Each cloud is flanked by two control windows: one below the base and one above the top, each offset from the cloud boundaries by 180 m and extending for 600 m. Within each window we evaluate:

200 – a symmetry condition

$$S = \left| \frac{\langle R_{\text{up}} \rangle - \langle R_{\text{down}} \rangle}{\langle R_{\text{up}} \rangle + \langle R_{\text{down}} \rangle} \right| < 0.10,$$

– a homogeneity requirement  $\text{var}(R)/\text{mean}(R) < 0.10$  in both windows,

– a smoothness criterion  $|R_{i+1} - R_i| < 0.10$  for all adjacent bins,

– a relative depolarisation constraint

205 
$$d_{\text{rel}} = \frac{|\langle \delta_{\text{up}} \rangle - \langle \delta_{\text{down}} \rangle|}{(\langle \delta_{\text{up}} \rangle + \langle \delta_{\text{down}} \rangle)/2} < 0.10.$$

Only clouds satisfying all tests are retained. The subset therefore consists of layers surrounded by aerosol-free, vertically uniform air, for which the Young inversion is expected to provide unbiased estimates of the lidar ratio. Presenting results from both data sets is thus essential: the full set captures the climatological LR variability across all microphysical regimes, whereas the Young–optimised subset provides a physically conservative benchmark of conditions for which the Young inversion is  
210 deemed more reliable.

The purpose of these criteria is not to optimise the retrieved lidar ratio toward specific numerical values, but to isolate cloud layers for which the Young inversion is expected to be most internally consistent. Although the numerical thresholds adopted here are necessarily empirical, the resulting reduction of structural complexity, high and variable background on which the cloud insists and the preferential exclusion of vertically inhomogeneous layers whose inversion could induce curvatures in the  
215 cloud-free profiles, are robust features that do not depend sensitively on moderate variations of the selected limits.



#### 4 Statistical analysis

The dataset spans 144 measurement days in 2022, 90 in 2023, and 112 in 2024. However, the statistical analyses presented in this work are based on individual cloud layers identified within each measurement, rather than on the number of measurement days. Each detected cloud layer represents one independent realisation for the lidar-ratio retrieval.

220 The final Young-inverted products consist of vertically resolved profiles of lidar ratio (LR), backscatter ratio  $R_{\text{def},\text{volume}}$  depolarization  $\delta$ , particle depolarisation  $\delta_A$ , aerosol backscatter coefficient  $\beta_{\text{aer}}$  in 60 m altitude bins, together with uncertainties, and diagnostic flags. For the statistical analysis we distinguish two cloud populations based on altitude: (i) tropospheric cirrus, defined as layers located below the climatological tropopause (12 km) (Snels et al., 2021; Ricaud et al., 2020) and (ii) polar stratospheric clouds (PSCs) located above this level. A sensitivity analysis was performed by varying the tropopause  
225 height by  $\pm 2$  km, which did not produce significant changes in the resulting LR statistics or in the classification of cloud types.

To separate the main PSC microphysical regimes we adopt simple, physically-based thresholds in  $R_{\text{def}}$  and  $\delta_A$ . These criteria are chosen to isolate the “core” regions of each class while minimising overlap in transitional areas. The classification of PSC microphysical classes is based on physically motivated thresholds in backscatter ratio and depolarisation, consistent  
230 with previous analyses at Dome C and long-term lidar observations (Snels et al., 2021; Di Liberto et al., 2026; Serva et al., 2026).

- **STS:**  $1.2 \leq R_{\text{def}} \leq 3$  and  $\delta_{\text{TA}} < 0.05$  occurring above the tropopause

This region corresponds to nearly spherical ternary-solution droplets, characterised by very low depolarisation and moderate backscatter enhancement.

- 235
- **NAT:**  $1.2 \leq R_{\text{def}} \leq 3$  and  $\delta_{\text{TA}} > 0.10$  occurring above the tropopause.

NAT particles produce intermediate depolarisation ( $\sim 0.1$ – $0.3$ ), typically with modest backscatter ratios compared to ice PSC.

- **Ice PSC:**  $R_{\text{def}} \geq 3$  and  $\delta_{\text{TA}} > 0.15$  occurring above the tropopause.

240 These thresholds identify highly aspherical crystalline ice with strong depolarisation and large backscatter enhancement, often associated with mesoscale temperature perturbations or deep synoptic excursions.

- **Tropospheric cirrus:**  $R_{\text{def}} \geq 3$  and  $\delta_{\text{TA}} > 0.15$ , but occurring below the tropopause.

This criterion isolates well-developed ice clouds in the upper troposphere, with optical signatures that overlap those of ice PSC but are distinguished by their altitude and thermodynamic environment.

245 These classification masks are deliberately conservative: they retain only the central, least ambiguous regions of each microphysical class and leave transitional cases unclassified. This approach is well suited for lidar-ratio climatology because the LR variability may be largest in mixed-phase or transitional regimes, which would broaden the statistical distributions without improving their physical interpretability.



#### 4.1 Optical weighting of the layer-mean lidar ratio

For each detected cloud, the Young inversion provides a single lidar ratio value LR representative of the entire layer, which is  
250 therefore assigned identically to every 60 m vertical sample belonging to that cloud. However, different portions of the cloud  
do not contribute equally to its optical depth. The cloud core, where  $\beta_{\text{aer}}$  is largest, dominates the total extinction, whereas  
tenuous peripheral regions contribute comparatively little.

To reflect this internal structure when compiling LR statistics over many measurements, we assign an optical weight to each  
60 m vertical sample within a cloud,  $w(z) \propto \beta_{\text{aer}}(z)$  with the weights normalised so that  $\sum_{z \in \text{cloud}} w(z) = 1$ . These weights do  
255 *not* modify the LR assigned to the cloud: the Young inversion always yields a single LR per cloud. Instead, the weights are used  
exclusively in the statistical analysis to regulate how each part of the cloud contributes to the LR distributions. In practice, this  
means that every cloud contributes equally to the overall climatology (because the normalised weights always sum to unity),  
but the portions of each cloud that carry the largest share of its optical thickness contribute proportionally more to the statistical  
aggregates. Thin boundary segments have smaller weights and therefore exert a correspondingly smaller influence on the LR  
260 histograms, PDFs and two-dimensional distributions. This approach ensures that the climatological LR statistics are governed  
primarily by the optically dominant regions of the cloud population while retaining the single-layer LR definition imposed by  
the Young inversion.

Because the optical weighting is normalised within each cloud layer, the statistical robustness of the results primarily depends  
on the number of analysed cloud layers rather than on the number of individual range bins or profiles.

265 The dependence of LR on microphysical state is investigated using two-dimensional histograms. The variables  $1 - 1/R$   
and  $\delta_T$  provide a compact description of the optical regime, as in this transformed space, clouds characterized by the same  
intrinsic aerosol depolarization align along straight lines, and  $\delta_{TA}$  is found on the far-right side of the plot, where the molecular  
contribution becomes negligible and the observed signal reflects only the aerosol scattering properties. This greatly facilitates  
the interpretation of the lidar signal separating spherical STS particles, moderately depolarizing NAT mixtures, and highly  
270 aspherical ice crystals. For each  $1 - 1/R, \delta_T$  bin, we compute the average of the optically weighted LR:

$$LR_w(1 - 1/R, \delta_T) = \frac{\sum w_i LR_i}{\sum w_i},$$

requiring a minimum number of points per bin for reliable statistics. This produces a microphysically interpretable map of  
LR in the  $1 - 1/R$  and  $\delta_T$  space for both cirrus and PSCs.

275 Optically weighted probability density functions (PDFs) of LR are computed separately for cirrus, STS, NAT and ice PSCs,  
using the microphysical thresholds defined in Sect. 3.11. The resulting PDFs provide robust mean LR values and spread for  
each class, suitable for comparison with climatological values reported in the literature.

LR distributions computed using the full dataset and the Young-optimized are evaluated. The comparison between full and  
filtered datasets provides a quantitative estimate of the systematic bias introduced when possible aerosol asymmetries above or  
below clouds are present.



280 Table 1 summarises the number of cloud layers contributing to each microphysical class for the full dataset and for the Young-optimized subset.

## 5 Results

In this section we present the LR statistics obtained from the Young inversion applied to three years of polarization lidar measurements at Concordia Station. The analysis is structured by cloud type (PSCs and tropospheric cirrus) and, for each  
285 category, we compare the results obtained from the full dataset with those from the subset of profiles fulfilling the Young-optimized criteria.

For both PSC and cirrus, we analyse: (i) the distribution of measurements in the  $(1 - 1/R, \delta_T)$  phase space, (ii) the optically-weighted LR in the same space, and (iii) the one-dimensional PDF of LR.

### 5.1 Stratospheric Polar Stratospheric Clouds

290 Figure 1 shows the dataset point-density distribution in the  $(1 - 1/R, \delta_T)$  phase space for the full dataset (left) and for the Young-optimized subset (right). The full dataset exhibits the expected tripartition of PSC microphysical types. Using the classification thresholds introduced in Sect. 4 — STS for  $1.2 \leq R \leq 3$  and  $\delta_{TA} < 0.05$ , NAT for  $1.2 \leq R \leq 3$  and  $\delta_{TA} > 0.10$ , and ice PSC for  $R \geq 3$  and  $\delta_{TA} > 0.15$  — the three regimes appear as well-separated clusters.

In the full dataset, the distribution shows points in the lower-left region ( $1 - 1/R < 0.8$ ,  $\delta_{TA} < 0.05$ ), corresponding to STS  
295 layers. This dense accumulation reflects the high frequency of STS conditions in the polar vortex and the fact that STS droplets produce only modest enhancements in backscatter and minimal depolarisation.

In the  $(1 - 1/R, \delta_T)$  space, straight lines emanating from the origin points towards a given value of  $\delta_T = \delta_{TA}$  for  $R = \infty$ , and represent data from clouds with approximately constant microphysical morphology and increasing optical thickness (Adachi et al., 2001). The elongated diagonal cluster that occupies the intermediate depolarisation range ( $\delta_{TA} \approx 0.05$ – $0.15$ ) and spans  
300  $1 - 1/R \approx 0.2$ – $0.6$  can therefore be interpreted as coming from a sequence of NAT with similar particle habits but progressively larger optical depth, whose nonspherical particles increase both backscatter ratio and total depolarisation in a correlated manner, producing the observed tilted distribution.

A third, more diffuse lobe extends toward high values of both axes ( $1 - 1/R > 0.6$ ,  $\delta_T > 0.15$ ), marking ice PSC. The broad spread in this region reflects the wide variability of optical thickness, ice crystal habits and sizes, particularly under mesoscale  
305 cooling or in strongly supersaturated conditions. The patchier appearance of this region is a consequence of the relative rarity and intrinsic inhomogeneity of ice PSC, which often feature sharp vertical gradients and sublayering in externally mixed clouds.

In the Young-optimized subset, the distribution collapses into the lower portion of the diagram, with almost all ice PSC occurrences removed. The subset retains mainly STS and NAT layers, and even within the NAT regime the distribution becomes  
310 more compact. This reduction is a direct consequence of the Young homogeneity criteria: ice PSC commonly exhibit strong vertical gradients, multilayer structures, and abrupt transitions in both  $R$  and  $\delta_T$ , which violate the symmetry, homogeneity,



and smoothness conditions described in Sect. 3.10. The subset therefore isolates the most vertically uniform PSC — chiefly extensive STS and NAT layers embedded in homogeneous, aerosol-free background air.

We attribute this near-disappearance of ice PSC in the Young-optimized subset to the difficulty to identify an ice PSC as  
315 an isolated layer, since these clouds tend to appear embedded within more complex PSC systems that include different cloud types. This is consistent with long-term lidar observations at other Antarctic sites. For example, the McMurdo PSC climatology of Adriani et al. (2004) documents that ice PSC exhibit a high degree of spatial and vertical variability, often appearing as thin, rapidly evolving layers embedded within or adjacent to other PSC types. These clouds frequently show sharp gradients in backscatter and depolarisation and are commonly associated with strong mesoscale temperature fluctuations. As a result, the  
320 atmospheric layers immediately above and below the cloud rarely satisfy the smooth, quasi-molecular conditions required by the Young optimization criteria.

In contrast, STS and NAT layers tend to be more vertically uniform and display more gradual transitions to the background aerosol, making them far more likely to fulfil the symmetry, smoothness and homogeneity constraints (Sect. 3.10). Thus, the Young-optimized subset naturally favours optically and dynamically simple layers, while filtering out the structurally complex  
325 and highly variable ice PSC identified in previous Antarctic climatologies (Santacesaria et al., 2001; Adriani et al., 2004).

To explore the dependence of the LR on backscatter and depolarization, we show in figure 2 the optically-weighted LR in the  $(1 - 1/R, \delta_T)$  phase space. In this figure and similarly in figure 6 the term “weighted number of events” refers to a statistical representation in which each detected cloud layer contributes a single lidar ratio (LR), distributed over its vertical extent with optical weights proportional to the aerosol backscatter coefficient. The weights are normalized within each cloud  
330 so that all clouds contribute equally to the statistics, while optically dominant regions within each cloud exert a larger influence than optically thin boundaries. For the full dataset on the left, LR increases with both backscatter and depolarisation, ranging from  $\sim 30$ – $50$  sr for STS,  $\sim 40$ – $70$  sr for NAT and for ice PSC. In the subset on the right panel, the NAT regime is preserved but the high-LR domain associated with ice PSC is almost entirely removed.

Figure 3 illustrates the LR probability distributions for the three PSC microphysical classes, comparing the full dataset (right)  
335 with the Young-optimized subset (left). In the full dataset, the three classes exhibit broad and partially overlapping distributions, reflecting both intrinsic microphysical variability and likely the frequent coexistence of multiple PSC types within the same vertical structure. STS show a relatively compact distribution centred around 38 sr (31–52 sr). NAT exhibits a wider spread, with a median of 50 sr (37–73 sr) and an extended high-LR tail. Ice PSC display the largest variability, ranging from  $\sim 20$  sr to very large values. This wide spread likely reflects not only the strong variability of crystal habits and growth conditions, but  
340 also the difficulty of isolating pure ice layers when they are embedded in mixed-phase structures; in such cases the retrieved LR represents an optical average over multiple particle populations, which tends to broaden the distribution and shift the median toward intermediate values.

In the Young-optimized subset, the LR distributions become markedly narrower for STS and NAT, while ice PSC nearly disappear because their edges typically show strong vertical inhomogeneities in both backscatter and depolarisation, causing  
345 them to fail the Young homogeneity and symmetry constraints. STS retain values around 41 sr (31–61 sr), but their distribution exhibits a weak bimodality. A first peak appears near 35 sr, consistent with classical supercooled ternary solution droplets



composed of  $\text{H}_2\text{SO}_4/\text{HNO}_3/\text{H}_2\text{O}$ . A second, smaller accumulation emerges around 60 sr. This higher-LR mode may reflect layers where STS droplets coexist with a minor fraction of nascent NAT particles, or where enhanced droplet growth under very cold conditions increases the extinction-to-backscatter ratio. Such mixed or transitional regimes are difficult to isolate in the full dataset, but the Young filtering suppresses many complex profiles and thus makes this subtle structure more visible.

NAT displays a clearer bimodal behaviour, with one mode around 40 sr and a second around 65–75 sr. This likely corresponds to the coexistence of two distinct NAT microphysical regimes: small, weakly depolarising NAT crystals and larger, highly aspherical NAT particles that form at very low temperatures. In the full dataset these subpopulations are partially masked by the presence of mixed or vertically structured PSC layers; the Young filtering seem to reveal this subdivision more distinctly.

The ice PSC distribution in the Young subset is extremely compressed (32–38 sr), indicating that only marginal cases survive the selection as their strong vertical gradients and likely external mixing with other classes of PSC make them incompatible with the Young inversion constraints.

It is important to stress that the low median LR retrieved for ice PSC in the Young-optimized subset should not be interpreted as representative of typical ice PSC conditions. Rather, it reflects the strong selection against vertically inhomogeneous and multi-layer ice clouds inherent to the Young filtering, which preferentially retains only marginal, optically simple cases.

Overall, the comparison between the two datasets reveals that: (i) the full dataset captures the complete diversity of PSC optical behaviour, including mixed-phase and multi-layer structures; (ii) the Young-optimized subset isolates the most homogeneous and vertically uniform PSC layers, yielding tighter LR distributions and exposing microphysical substructures — such as the apparent bimodality in both STS and NAT — that are not easily discernible in the full dataset.

It is important to stress that the lidar-ratio values obtained from the Young-optimized subset should not be interpreted as a replacement for the full climatological distributions. Instead, the two datasets provide complementary information: the full dataset comprehends the effective lidar-ratio variability encountered in real atmospheric conditions, including mixed-phase and multilayer clouds, whereas the Young-optimized subset offers a lower-bound, physically conservative estimate applicable to idealised, vertically homogeneous layers.

Given the very limited number of cloud layers retained in the Young-optimized subset, no statistically meaningful analysis of their temporal distribution or of their association with specific dynamical or climatological conditions can be performed. The subset should therefore be interpreted strictly as a methodological benchmark, highlighting the behaviour of the Young inversion under near-ideal conditions, rather than as a representative sample of particular atmospheric states.

Figure 4 shows the vertical evolution of the median lidar ratio (LR) and its interquartile range for the three PSC classes. Only the full data set is discussed in terms of vertical variability, since the number of Young-optimized cases becomes too small at several altitudes to support a statistically representative profile.

In the full data set, STS layers exhibit relatively low LR values (typically 35–45 sr) throughout the stratosphere, with a weak dependence on altitude up to about 22 km and a tendency toward slightly larger values at higher levels. This vertical stability reflects the microphysical nature of STS droplets, whose composition and size distribution evolve smoothly with temperature, yielding nearly constant optical properties over the probed altitude range.



NAT clouds display a broader LR distribution and a positive gradient with altitude, with median values increasing from  $\sim 40$  sr near 10–12 km to  $\sim 55$ –60 sr above 20 km. This behaviour is consistent with the increase in NAT particle growth efficiency at lower temperatures in the upper stratosphere, favouring larger and more aspherical particles with enhanced extinction-to-backscatter ratios. The relatively coherent vertical progression also reflects the dominant occurrence of NAT over a wide  
385 altitude range.

Ice PSC show the largest variability and no simple monotonic trend. Median LR values span from about 45 sr to more than 70 sr, with substantial scatter at all altitudes. Such variability is expected, as ice PSC often form in dynamically complex environments influenced by rapid mesoscale temperature fluctuations, and multi-layer embedded structures. As frequently reported in PSC climatologies, ice layers may coexist with NAT or STS in vertically interleaved configurations, making the  
390 isolation of pure ice layers difficult. The broad LR distribution therefore reflects not only the intrinsic variability of ice crystal habits and growth histories, but also possible contamination from adjacent mixed-phase structures, which can bias LR toward intermediate values.

## 5.2 Tropospheric Cirrus

The cirrus classification uses the same optical thresholds as ice PSC ( $R_{\text{def}} \geq 3$  and  $\delta_T > 0.15$ ), but restricted to altitudes below  
395 the climatological tropopause (12 km).

Figure 5 compares the point–density distribution in the  $(1 - 1/R, \delta_T)$  phase space for tropospheric clouds, shown for the full dataset (right panel) and the Young–optimized subset (left panel). The full dataset exhibits the expected continuum of microphysical states for tropospheric cirrus. The oblique lines radiating from the axis origin represent clouds of constant particle depolarisation  $\delta_A$ : along these trajectories the microphysical shape indicator is preserved while  $R$  increases. The  
400 figure shows that cirrus occupy a single continuous branch in  $(1 - 1/R, \delta_T)$  with particle depolarisation between 0.2 and 0.45, typically 0.30. The particle backscattering  $\beta_{\text{aer}}$ , not reported, spans over two orders of magnitude  $10^{-4}$ – $10^{-2}$   $\text{km}^{-1} \text{sr}^{-1}$ , representative of medium to high optical thickness cirrus clouds (Chazette et al., 2001).

In the Young–optimized subset (left panel), the number of available cases is significantly reduced. This reduction is expected and is primarily driven by the comparatively low signal-to-noise ratio of our tropospheric channels: the Young inversion re-  
405 quires well-defined cloud boundaries and smooth, extinction-corrected profiles both above and below the cloud, conditions that are often not met due to noisiness in our dataset. As a consequence, only the most structurally homogeneous, noise-free cirrus layers survive the Young criteria.

Despite the smaller sample, the locus of points retained by the Young selection remains consistent with the morphology of the full dataset: the same positive correlation between  $\delta_T$  and  $1 - 1/R$  is observed, and the high-density region corresponds  
410 to the same domain characteristic of mid-latitude cirrus. Overall, the comparison shows that: (i) the Young method does not introduce a systematic bias in the microphysical phase space of tropospheric clouds, and (ii) the reduced population mainly reflects S/N limitations rather than a physical filtering of specific cirrus types.

Figure 6 shows the distribution of tropospheric measurements coloured by the optically weighted mean lidar ratio (LR). The right panel corresponds to the full dataset, while the left panel shows only those cloud layers that satisfy all Young inversion



415 constraints. Across this full range, LR values span approximately 20–80 sr, consistent with climatological cirrus studies (e.g. Chen et al., 2002; Yorks et al., 2011; Giannakaki et al., 2007). A weak increase of LR toward higher depolarisation is also visible, perhaps reflecting the tendency of larger and more complex ice crystals to exhibit higher extinction-to-backscatter ratios. The clustering of data at  $(1 - 1/R) \simeq 0.8\text{--}0.9$ , i.e.  $R \simeq 5\text{--}10$ , corresponds to the optically thickest cirrus layers in our sample and is associated with LR values  $R \simeq 50$ .

420 The Young-optimised subset (left panel) occupies a narrower region of the same phase space, forming a well-defined ridge of points aligned toward  $\delta_{TA} \simeq 0.30$  and a few other scattered points, with low to intermediate values of  $1 - 1/R$ . This contraction is expected, since the Young inversion filters out layers with insufficient signal-to-noise ratio—conditions at the boundaries of the cloud, that are common in the tropospheric channel. Despite the reduced sampling, the LR distribution in the Young subset remains fully consistent with that of the full dataset. The retrieved values cluster tightly around 31–42 sr, not far from the the  
425 modal LR range seen in the unfiltered population. High-LR outliers ( $> 60$  sr) visible in the full dataset are absent. Overall, the comparison demonstrates that the Young-optimized subset is preserving the central microphysical signal of the full dataset. The modal LR is unchanged, and the phase-space structure (in particular the organisation along oblique lines of constant particle depolarisation) is maintained.

Figure 7 shows the probability density function (PDF) of the lidar ratio (LR) for tropospheric cirrus, respectively for the  
430 Young-optimized subset (right) and for the full tropospheric data set (left).

In the Young-optimized subset, the LR distribution is extremely compact, with a median value of  $\sim 41$  sr and an interquartile range confined to  $\sim 31\text{--}42$  sr. The narrowness of the distribution reflects the paucity of the dataset induced by the stringent homogeneity requirements of the Young inversion and is likely not representative of the whole variability of the LR. The full data set displays a much broader LR distribution, with a median of  $\sim 51$  sr and an extended upper tail reaching 80 sr. This  
435 broader range is consistent with previous Raman-lidar climatologies, which report LR values of 20–40 sr for thin cirrus and 40–70 sr (or higher) for vertically extended or multi-layer structures. The larger LR values in the full population may likely correspond to clouds with strong internal variability or large, complex ice habits such as bullet rosettes or aggregates, which increase the extinction-to-backscatter ratio, although biases induced by the Young inversion procedure can not be excluded. The vertical profiles (Fig. 8) show a slight decrease of LR with height, consistent with smaller particles near cloud top, likely linked  
440 to a reduced availability of water vapour. -

## 6 Discussion

The Young inversion relies on the assumption that the particle backscatter ratio is identical immediately above and below an homogeneous cloud layer. This condition is often met for vertically homogeneous layers (e.g. extended STS or NAT PSC, or thick homogeneous cirrus), but it can be severely violated in the presence of sharp vertical gradients and multiple sublayers,  
445 such as for ice PSC or dynamically perturbed cirrus. The comparison between the full data set and the Young-optimized subset therefore is aimed at providing a direct, observation-based quantification of how real polar clouds depart from these ideal



assumptions, and how such departures bias the retrieved lidar ratio. Unfortunately, for tropospheric ice clouds, the Young-optimized dataset is probably too sparse to be statistically significant.

An increase in the lidar ratio generally reflects a shift toward larger or more aspherical particles. Since the extinction coefficient scales approximately with particle cross-section while the relative backscatter efficiency decreases for larger or more complex particles, the ratio  $\alpha/\beta$  increases as particle size grows. This behaviour is well established in modelling studies for STS (Luo et al., 2003), NAT (Höpfner et al., 2006), and ice PSC (Reichardt et al., 2004), where higher LR values correspond to particles with larger effective radii or broader size distributions, or aspherical. Therefore, the observed increase of LR with altitude for NAT, and the large LR variability of ice PSC, are consistent with the presence of progressively larger or more complex particles under colder stratospheric conditions.

The PSC populations are cleanly separated in the  $(1 - 1/R, \delta_T)$  phase space, with STS at low depolarisation, NAT at intermediate values, and ice PSC at high depolarisation and larger variability. The optically weighted lidar ratios obtained from the full data set cluster around

$$LS_{STS} \approx 38 \text{ sr}, \quad LS_{NAT} \approx 50 \text{ sr}, \quad LS_{ice} \approx 52 \text{ sr},$$

with ice PSC spanning a broad range extending up to  $\sim 70$  sr. These values fall squarely within the microphysically expected regimes: Mie calculations predict STS droplets to exhibit LR in the 30–40 sr range with weak sensitivity to size and composition (Luo et al., 2003; Peter and Groö, 2012), while irregular NAT particles generally yield LR between 40 and 60 sr (Reichardt et al., 2004; Höpfner et al., 2006). Ice PSC show the largest variability due to the strong dependence of crystal habit and size on cooling history, sedimentation and mesoscale temperature variability (Reichardt et al., 2004; Tritscher et al., 2021).

The Young-optimized subset selectively removes layers where the Young inversion is more likely to fail. As a result, a modest shift is observed:

$$LS_{STS} \approx 41 \text{ sr}, \quad LS_{NAT} \approx 61 \text{ sr}, \quad LS_{ice} \approx 32 \text{ sr}.$$

The narrowing of LR for STS and NAT is expected as the Young inversion intrinsically favours clouds with a high degree of vertical uniformity and the substantial reduction in the ice-PSC median LR (from  $\sim 50$  to  $\sim 32$  sr) may reflect the systematic exclusion of multi-layer ice PSC.

Although the Young-optimized criteria are applied to regions outside the cloud, they are sensitive to inconsistencies introduced by the inversion within the cloud layer. If the cloud were a single, vertically homogeneous layer, the extinction correction based on a trial LR would modify the attenuated signal in a smooth and self-consistent manner, yielding nearly identical values of the corrected backscatter ratio above and below the cloud. In contrast, when a cloud contains internal sublayers with different extinction-to-backscatter ratios, no single LR can adequately describe the entire layer. The inversion is then forced to compensate by overcorrecting one part of the cloud and undercorrecting another, with these errors propagating into the extinction-corrected signal outside the cloud (Ansmann et al., 1990). As a result, the corrected backscatter ratio becomes asymmetric above and below the cloud and exhibits enhanced variance and gradients in the external control windows.

Therefore, the external Young criteria can also be interpreted as a sensitive indicator of internal cloud inhomogeneity: clouds that fail the tests are those for which the assumption of a single, physically meaningful LR is no longer valid. For practical



applications, these results suggest that lidar-ratio climatologies intended for radiative-transfer modelling, satellite validation, or long-term statistics should rely on the full dataset, which reflects not only the diversity of real cloud structures but also the uncertainties and methodological biases inherent to elastic-lidar retrievals.

The LR values retrieved in this work are consistent with previous lidar studies. Early ground-based Raman and depolarisation  
485 lidar measurements reported 30–40 sr for STS and 40–60 sr for NAT or mixed-phase PSC (Reichardt et al., 2004, 2002), with  
ice PSC occasionally exceeding 60 sr during intense mountain-wave events. CALIOP climatologies similarly employ type-  
dependent LR values of 30 sr (STS), 50 sr (NAT) and 25–60 sr (ice), depending on layer structure (Pitts et al., 2009, 2018).  
At Concordia, previous PSC studies primarily characterised the backscatter–depolarisation phase space (Snels et al., 2021;  
Di Liberto et al., 2024), and the present analysis extends this framework by adding quantitative LR retrievals, confirming the  
490 internal consistency between microphysical typing and optical properties.

Tropospheric cirrus above Dome C exhibit median LR values of  $LR_{\text{cirrus}} \approx 51$  sr in the full data set, with a tail extending to  
lower values. These values are consistent with Raman lidar studies reporting typical visible-wavelength LR of 20–40 sr for thin  
cirrus and 40–50 sr for vertically extended or multi-layer clouds (Ansmann et al., 1992; Immler and Schrems, 2002; Haarig  
et al., 2016; Wang et al., 2020).

495 Under Young–optimized conditions, the median LR decreases to  $LR_{\text{cirrus}} \approx 41$  sr and the distribution narrows. The lower-  
bound value of  $\sim 30$  sr is physically consistent with homogeneous, optically simple cirrus and agrees with Raman-lidar obser-  
vations at other high-latitude sites, although the scarcity of data for the Young-optimized dataset suggest to pose some caution  
on the representativeness of such results.

An interesting outcome is the difference between the LR of ice PSC and cirrus, despite both being composed of crystalline  
500 ice. Ice PSC observed above Dome C typically span 40–60 sr with excursions beyond 70 sr, while cirrus peak around 45–50 sr  
and rarely approach PSC-like values.

This contrast is consistent with their different microphysical pathways and with the effective optical complexity sampled by  
lidar observations. Ice PSC form at extremely low temperatures ( $T < 188$  K) through heterogeneous nucleation on pre-existing  
STS or NAT particles. As a consequence, ice PSC crystals are generally smaller than cirrus crystals but are expected to be  
505 highly aspherical and poorly constrained in habit. Their optical response is further complicated by frequent coexistence with  
NAT or STS layers and by strong vertical inhomogeneities, which can enhance the effective lidar ratio retrieved for the layer.

Conversely, cirrus clouds form either in situ or by convective detrainment in a warmer and moister environment, allowing  
the growth of larger ice crystals with well-developed habits (columns, plates, bullet rosettes, aggregates). Despite their larger  
size, cirrus layers are often optically more homogeneous, leading to more stable LR values and fewer extreme excursions.

510 Thus, the observed differences between PSC and cirrus LR can be physically explained by the combined effects of particle  
habit, mixing state, and vertical homogeneity, rather than by crystal size alone.



## 7 Conclusions

We presented a three-year dataset (2022–2024) of ground-based polar stratospheric cloud (PSC) and cirrus observations performed at Dome C using a polarization-diversity Rayleigh lidar. For the first time at this site, lidar ratios (LR) were retrieved systematically using the Young inversion method. The resulting dataset provides a physically consistent characterisation of PSC and cirrus optical properties and establishes a reference framework for future studies in Antarctica.

The retrieved LR distributions for the full PSC population peak around  $\sim 38$  sr for STS,  $\sim 50$  sr for NAT, and  $\sim 52$  sr for ice PSC, with percentiles spanning the ranges (31–52), (37–73), and (40–65) sr, respectively. These values are consistent with expectations from optical modelling and with previous Raman and depolarisation lidar studies. Importantly, the broad LR distribution of ice PSC is likely not only a signature of intrinsic microphysical variability, but also a consequence of their frequent coexistence with STS and NAT within mixed-phase structures. Under such conditions, retrieving a single, layer-integrated LR inevitably leads to values that represent an aggregate of multiple particle types rather than a pure ice signature.

Tropospheric cirrus exhibit median lidar ratios of  $\sim 49$  sr (34–52 sr), with the Young-compatible subset converging toward lower values around  $\sim 41$  sr.

Joint analysis in the  $(1 - 1/R, \delta_T)$  space confirms the clear separation of PSC regimes and the tight clustering of cirrus. The observed distributions agree with theoretical phase-space structures: lines of constant particle depolarisation correspond to families of optically thickening clouds, while the elongation of the NAT cluster reflects increasing optical depth at nearly constant morphology.

Overall, this work provides a long-term, internally consistent statistic of PSC and cirrus lidar ratios at Dome C and a quantitative assessment of how real clouds retrievals deviate from the assumptions underlying the Young method. An important implication of this analysis is that lidar-ratio statistic cannot be uniquely defined without reference to the validity of the underlying inversion assumptions. By explicitly distinguishing between full and Young-optimized datasets, this work provides both a realistic representation of the variability encountered in operational conditions and a conservative benchmark applicable to idealized homogeneous cloud layers.

The dataset and methods developed here may support ongoing efforts to evaluate PSC microphysical transitions, diagnose stratospheric temperature anomalies, and improve spaceborne lidar retrievals in polar regions.

A key outcome of this work is therefore not a single set of lidar-ratio values, but a quantitative framework that links lidar-ratio statistics to the validity of the underlying inversion assumptions. This framework enables a transparent and physically consistent use of ground-based lidar observations in both climatological and methodological contexts. The LR statistic presented here also provides a useful ground-based reference for the interpretation of upcoming spaceborne lidar observations, particularly in the context of the EarthCARE mission and its ATLID instrument. Recent studies have started to report the first EarthCARE observations of PSCs, and the availability of independent, long-term ground-based LR statistics will be valuable for validation and for refining PSC classification schemes.



*Code and data availability.* The data sets and analysis codes used in this study are available from the authors upon request. The PSC-related  
545 lidar data are publicly available through the NDACC data archive at <https://ndacc.larc.nasa.gov/instruments/lidar>.

*Author contributions.* FC and MS processed the data and performed the analysis. LDL and AB operated the system and collected the data. FC wrote the manuscript with contributions from all authors.

*Competing interests.* The authors declare that they have no competing interests.

*Acknowledgements.* The authors acknowledge the financial support by PNRA for the Concordia lidar observatory in the framework of the  
550 projects Osservatorio Lidar a Dome Concordia (PNRA14\_00127) and LIDAROBS and the support of the ISSI-PSC initiative project.

Logistical and winter-time technical assistance was provided by the Piano Nazionale della Ricerca in Antartide (PNRA).

The authors thank Angelo Galeandro, Davide Carlucci and Mario Lecca for performing the ground-based lidar measurements at Dome C during the winter and Maurizio Viterbini and Ilir Shuli for their valuable technical expertise.



## References

- 555 Achtert, P., Khaplanov, M., Khosrawi, F., et al.: Properties of a subvisible midlevel cloud observed during a SAGE III/ISS validation campaign, *Atmospheric Chemistry and Physics*, 13, 12 269–12 279, <https://doi.org/10.5194/acp-13-12269-2013>, 2013.
- Adachi, H., Shibata, T., Iwasaka, Y., and Fujiwara, M.: Calibration method for the lidar-observed stratospheric depolarization ratio in the presence of liquid aerosol particles, *Appl. Opt.*, 40, 6587–6595, <https://doi.org/10.1364/AO.40.006587>, 2001.
- Adriani, A., Massoli, P., Di Donfrancesco, G., Cairo, F., Moriconi, M., and Snels, M.: Climatology of polar stratospheric clouds based on  
560 lidar observations from 1993 to 2001 over McMurdo Station, Antarctica, *Journal of Geophysical Research: Atmospheres*, 109, D24 211, <https://doi.org/10.1029/2004JD004932>, 2004.
- Ansmann, A., Riebesell, M., and Weitkamp, C.: Measurement of atmospheric aerosol extinction profiles with a Raman lidar, *Opt. Lett.*, 15, 746–748, <https://doi.org/10.1364/OL.15.000746>, 1990.
- Ansmann, A., Wandinger, U., Riebesell, M., Weitkamp, C., and Michaelis, W.: Independent measurement of extinction and  
565 backscatter profiles in cirrus clouds using a combined Raman elastic-backscatter lidar, *Applied Optics*, 31, 7113–7131, <https://doi.org/10.1364/AO.31.007113>, 1992.
- Behrendt, A. and Nakamura, T.: Calculation of the calibration constant of polarization lidar and its dependency on atmospheric temperature, *Opt. Express*, 10, 805–817, <https://doi.org/10.1364/OE.10.000805>, 2002.
- Böckmann, C. and Ritter, C.: Properties of Polar Stratospheric Clouds over the European Arctic from Ground-Based Lidar, in: *Proceedings of the 30th International Laser Radar Conference (ILRC 2022)*, edited by Sullivan, J. T. et al., Springer Atmospheric Sciences, pp. 325–332, Springer, Cham, [https://doi.org/10.1007/978-3-031-37818-8\\_43](https://doi.org/10.1007/978-3-031-37818-8_43), 2023.
- Cairo, F., Donfrancesco, G. D., Adriani, A., Pulvirenti, L., and Fierli, F.: Comparison of various linear depolarization parameters measured by lidar, *Appl. Opt.*, 38, 4425–4432, <https://doi.org/10.1364/AO.38.004425>, 1999.
- Cairo, F., Deshler, T., Di Liberto, L., Scoccione, A., and Snels, M.: A study of optical scattering modelling for mixed-phase polar stratospheric  
575 clouds, *Atmospheric Measurement Techniques*, 16, 419–431, <https://doi.org/10.5194/amt-16-419-2023>, 2023.
- Chazette, P., Pelon, J., and Mégie, G.: Determination by spaceborne backscatter lidar of the structural parameters of atmospheric scattering layers, *Appl. Opt.*, 40, 3428–3440, <https://doi.org/10.1364/AO.40.003428>, 2001.
- Chen, W. N., Chiang, C. W., and Nee, J. B.: Lidar ratio and depolarization ratio for cirrus clouds, *Applied Optics*, 41, 6470–6476, <https://doi.org/10.1364/AO.41.006470>, 2002.
- 580 Córdoba-Jabonero, C., Sorribas, M., Gil, M., et al.: Polar stratospheric cloud observations in the 2006/07 Arctic winter by using an improved micropulse lidar, *Applied Optics*, 52, 2980–2992, <https://doi.org/10.1364/AO.52.002980>, 2013.
- David, C., Bekki, S., Marchand, M., et al.: Evaluation of stratospheric ozone, temperature, and aerosol profiles from the LOANA lidar in Antarctica, *Journal of Atmospheric and Solar-Terrestrial Physics*, 74, 219–230, <https://doi.org/10.1016/j.jastp.2011.10.004>, 2012.
- Del Guasta, M.: Errors in the retrieval of thin-cloud optical parameters by lidar, *Applied Optics*, 37, 5522–5531, 1998.
- 585 Di Liberto, L., Snels, M., Cairo, F., et al.: Polar Stratospheric Cloud Observations at Concordia Station by the Remotely Controlled Lidar Observatory, *Remote Sensing*, 16, 2228, <https://doi.org/10.3390/rs16122228>, 2024.
- Di Liberto, L., Colao, F., Serva, F., Bracci, A., Cairo, F., and Snels, M.: 10 years of lidar observations of polar stratospheric clouds at Concordia Station, *Remote Sensing*, under review, 2026.
- Giannakaki, E., Balis, D. S., Amiridis, V., and Kazadzis, S.: Optical and geometrical characteristics of cirrus clouds over a Southern European  
590 lidar station, *Atmospheric Chemistry and Physics*, 7, 5519–5530, <https://doi.org/10.5194/acp-7-5519-2007>, 2007.



- Gimmestad, G. G.: Reexamination of depolarization in lidar measurements, *Appl. Opt.*, 47, 3795–3802, <https://doi.org/10.1364/AO.47.003795>, 2008.
- Gobbi, G. P.: Lidar observations of polar stratospheric clouds at McMurdo station, Antarctica, *Journal of Geophysical Research: Atmospheres*, 100, 11 219–11 235, <https://doi.org/10.1029/95JD00725>, 1995.
- 595 Haairig, M., Ansmann, A., Gasteiger, J., et al.: 1064 nm Raman lidar for extinction and lidar ratio profiling of tropospheric aerosol and cirrus, *Atmospheric Measurement Techniques*, 9, 4269–4283, <https://doi.org/10.5194/amt-9-4269-2016>, 2016.
- Holz, R. E., Ackerman, T. P., Noh, Y.-J., et al.: An HSRL retrieval of cirrus cloud optical and microphysical properties, *Applied Optics*, 41, 5870–5883, <https://doi.org/10.1364/AO.41.005870>, 2002.
- Höpfner, M., Luo, B. P., Massoli, P., Cairo, F., Spang, R., Snels, M., Stiller, G., von Clarmann, T., Fischer, H., Biermann, U. M., and Peter, T.: Spectroscopic evidence for NAT, STS, and ice in polar stratospheric clouds, *Atmospheric Chemistry and Physics*, 6, 1201–1219, <https://doi.org/10.5194/acp-6-1201-2006>, 2006.
- 600 Hostetler, C. A., Liu, Z., and Reagan, J.: CALIOP Algorithm Theoretical Basis Document: Calibration and Level 1 Data Products, Tech. Rep. PC-SCI-201, NASA, 2006.
- Immler, F. and Schrems, O.: LIDAR measurements of cirrus clouds in the northern and southern midlatitudes during INCA: A comparative study, *Geophysical Research Letters*, 29, 56–1–56–4, <https://doi.org/10.1029/2002GL015077>, 2002.
- 605 Iwabuchi, H. et al.: Effects of Cloud Horizontal Inhomogeneity on Optical Retrievals, *Journal of Atmospheric Sciences*, 59, 1520–1534, 2002.
- Josset, D., Pelon, J., Hu, Y., and Zhai, P. W.: Multi-instrument calibration method for hybrid extinction and backscatter lidar: application to spaceborne measurements, *Journal of Geophysical Research: Atmospheres*, 117, D05 205, <https://doi.org/10.1029/2011JD016959>, 2012.
- 610 Kim, M.-H., Omar, A. H., Tackett, J. L., et al.: CALIPSO version 4 automated aerosol classification and lidar ratio selection algorithm, *Atmospheric Measurement Techniques*, 11, 6107–6135, <https://doi.org/10.5194/amt-11-6107-2018>, 2018.
- Lolli, S., Dolinar, E. K., Lewis, J. R., Salcedo-Bosch, A., Campbell, J. R., and Welton, E. J.: Long-term trends in daytime cirrus cloud radiative effects: Analyzing twenty years of Micropulse Lidar Network measurements at Greenbelt, Maryland in eastern North America, *EGUsphere*, 2025, 1–23, <https://doi.org/10.5194/egusphere-2025-1237>, 2025.
- 615 Luo, B. P., Voigt, C., Fueglistaler, S., and Peter, T.: Extreme NAT supersaturations in mountain wave ice polar stratospheric clouds: A clue to NAT formation, *Journal of Geophysical Research: Atmospheres*, 108, 4441, <https://doi.org/10.1029/2002JD003104>, 2003.
- Nakoudi, K., Stachlewska, I. S., and Ritter, C.: An extended lidar-based cirrus cloud retrieval scheme: first application over an Arctic site, *Optics Express*, 29, 8553–8578, <https://doi.org/10.1364/OE.419914>, 2021.
- Noel, V., Hertzog, A., and Chepfer, H.: CALIPSO observations of wave-induced PSCs with near-unity optical depth over Antarctica in 2006–2007, *Journal of Geophysical Research: Atmospheres*, 114, <https://doi.org/https://doi.org/10.1029/2008JD010604>, 2009.
- 620 Peter, T. and Grooß, J.-U.: Polar Stratospheric Clouds and Sulfate Aerosol Particles: Microphysics, Denitrification and Heterogeneous Chemistry, in: *Stratospheric Ozone Depletion and Climate Change*, edited by Newman, A. L., pp. 108–144, Royal Society of Chemistry, Cambridge, UK, <https://doi.org/10.1039/9781849733182-00108>, 2012.
- Pitts, M. C., Poole, L. R., and Thomason, L. W.: CALIPSO polar stratospheric cloud observations: Second-generation detection algorithm and composition discrimination, *Atmospheric Chemistry and Physics*, 9, 7577–7589, <https://doi.org/10.5194/acp-9-7577-2009>, 2009.
- 625 Pitts, M. C., Poole, L. R., and Gonzalez, R.: Polar stratospheric cloud climatology based on CALIPSO spaceborne lidar measurements from 2006 to 2017, *Atmospheric Chemistry and Physics*, 18, 10 881–10 913, <https://doi.org/10.5194/acp-18-10881-2018>, 2018.



- Reichardt, J., Reichardt, S., and et al.: Retrieval of polar stratospheric cloud microphysical properties from lidar measurements: Dependence on particle shape assumptions, *Journal of Geophysical Research*, 107, 8270, <https://doi.org/10.1029/2001JD001021>, 2002.
- 630 Reichardt, J. et al.: Mountain wave PSC dynamics and microphysics from ground-based lidar measurements, *Atmospheric Chemistry and Physics*, 4, 1149–1165, <https://doi.org/10.5194/acp-4-1149-2004>, 2004.
- Ricaud, P., Gabard, B., Derrien, S., Chaboureau, J.-P., Rose, T., Mombauer, A., and Crepulja, M.: Validation of Aura MLS temperature, water vapor, and ozone profiles in the Antarctic stratosphere using Concordia station radiosonde measurements, *Atmospheric Measurement Techniques*, 13, 111–130, 2020.
- 635 Santacesaria, V., Mackenzie, A. R., and Stefanutti, L.: A climatological study of polar stratospheric clouds (1989–1997) from LIDAR measurements over Dumont d’Urville (Antarctica), *Tellus B: Chemical and Physical Meteorology*, 53, 306–321, <https://doi.org/10.3402/tellusb.v53i3.16598>, 2001.
- Serva, F., Di Liberto, L., Colao, F., Bracci, A., Cairo, F., Pitts, M. C., and Snels, M.: Impact of the Hunga eruption on polar stratospheric clouds as seen by the lidar observatory at Concordia Station, *Antarctic Science*, under review, 2026.
- 640 Snels, M., Colao, F., Cairo, F., Shuli, I., Scoccione, A., De Muro, M., Pitts, M., Poole, L., and Di Liberto, L.: Quasi-coincident observations of polar stratospheric clouds by ground-based lidar and CALIOP at Concordia (Dome C, Antarctica) from 2014 to 2018, *Atmospheric Chemistry and Physics*, 21, 2165–2178, <https://doi.org/10.5194/acp-21-2165-2021>, 2021.
- Solomon, S.: Stratospheric ozone depletion: A review of concepts and history, *Reviews of Geophysics*, 37, 275–316, <https://doi.org/10.1029/1999RG900008>, 1999.
- 645 Tritscher, I., Peter, T., et al.: Polar stratospheric clouds: Satellite observations, processes, and role for ozone depletion, *Reviews of Geophysics*, 59, e2020RG000702, <https://doi.org/10.1029/2020RG000702>, 2021.
- Vaughan, M. A., Young, S. A., Winker, D. M., Powell, K. A., Omar, A., Liu, Z., Hu, Y., and Hostetler, C. A.: Fully automated analysis of space-based lidar data: An overview of the CALIPSO retrieval algorithms and data products, in: *Proc. SPIE 5575, Lidar Remote Sensing for Industry and Environment Monitoring*, pp. 16–30, <https://doi.org/10.1117/12.572024>, 2004.
- 650 Wang, W. et al.: Characteristics and seasonal variations of cirrus clouds derived from ground-based lidar observations, *Remote Sensing*, 12, 3998, <https://doi.org/10.3390/rs12233998>, 2020.
- Yorks, J. E., McGill, M. J., Hart, W. D., and Scott, S. G.: Evaluating cirrus cloud optical properties from NASA’s Cloud Physics Lidar (CPL), *Journal of Geophysical Research: Atmospheres*, 116, D00T07, <https://doi.org/10.1029/2010JD014906>, 2011.
- Young, S. A.: Analysis of lidar backscatter profiles in optically thin clouds, *Applied Optics*, 34, 7019–7031, <https://doi.org/10.1364/AO.34.007019>, 1995.
- 655 Young, S. A. and Vaughan, M. A.: The retrieval of profiles of particulate extinction from CALIPSO data: Theory and initial results, in: *Proceedings of the 24th International Laser Radar Conference*, 2009.

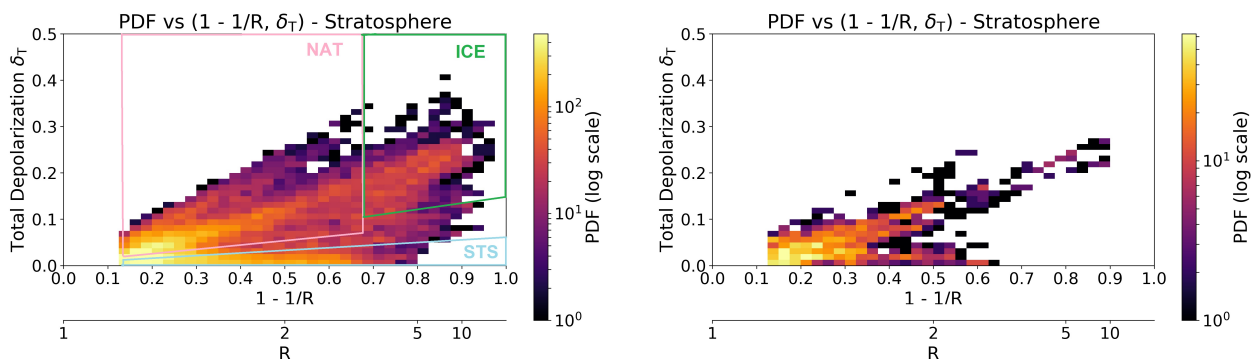


**Figure 1.** Point–density probability distribution of PSC measurements in the  $(1 - 1/R), \delta_T$  optical phase space. Left: full dataset including all Young-inverted cloud layers. Right: Young–optimized subset (Sect. 3.1). The full dataset cleanly separates STS, NAT and ice PSC clusters, while the Young–optimized subset suppresses most ice PSC occurrences. Regions identified as STS, NAT and ice PSCs are indicated by areas bounded by light-blue, pink and green contours, respectively.

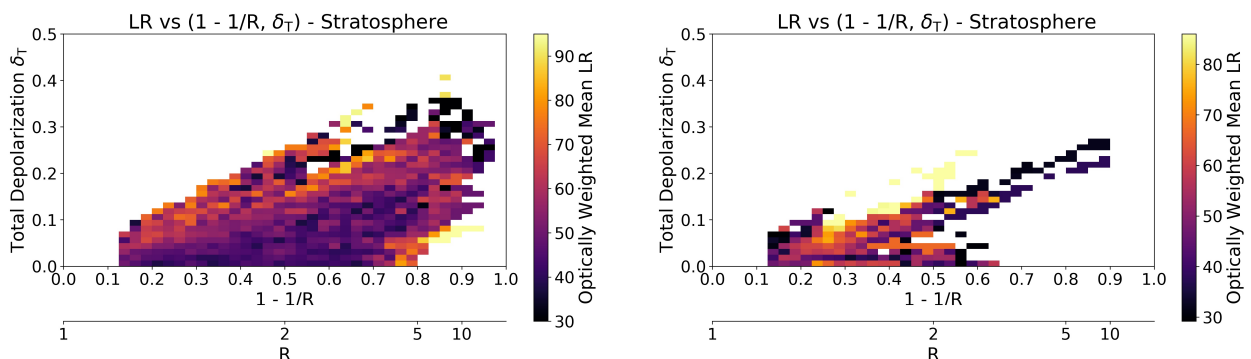


**Figure 2.** Optically–weighted mean lidar ratio (LR) in the  $(1 - 1/R), \delta_T$  phase space for PSC. Left: full dataset. Right: Young–optimized subset. LR increases with both backscatter enhancement and depolarization, with STS occupying the low-LR, weak-depolarization region, NAT forming an intermediate branch, and ice PSC reaching the largest LR values. In the Young–optimized subset most high-LR ice PSC disappear, likely because their cloud boundaries violate Young optimization conditions.

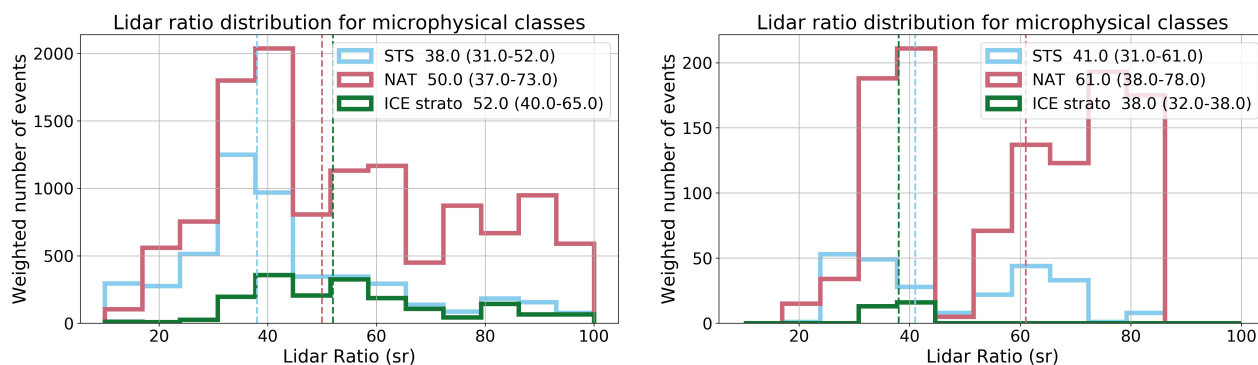


**Figure 3.** One-dimensional probability density functions (PDFs) of the lidar ratio (LR) for the three PSC microphysical classes: STS, NAT, and ice. Left: full dataset. Right: Young-optimized subset. The full dataset shows broad and partially overlapping distributions, especially for ice PSC due to their intrinsic microphysical variability and frequent embedding within mixed-phase structures. The Young subset yields narrower distributions for STS and NAT and retains only a few marginal ice PSC cases, illustrating the selective nature of the Young optimized criteria.

**Table 1.** Number of cloud layers contributing to the statistical analysis for the full dataset and for the Young-optimized subset. PSC classes include STS, NAT and ice; cirrus layers are listed separately.

Cloud class	Full dataset	Young-optimized
STS PSC	125	12
NAT PSC	136	12
Ice PSC	9	2
Total PSC	270	26
Tropospheric cirrus	107	2

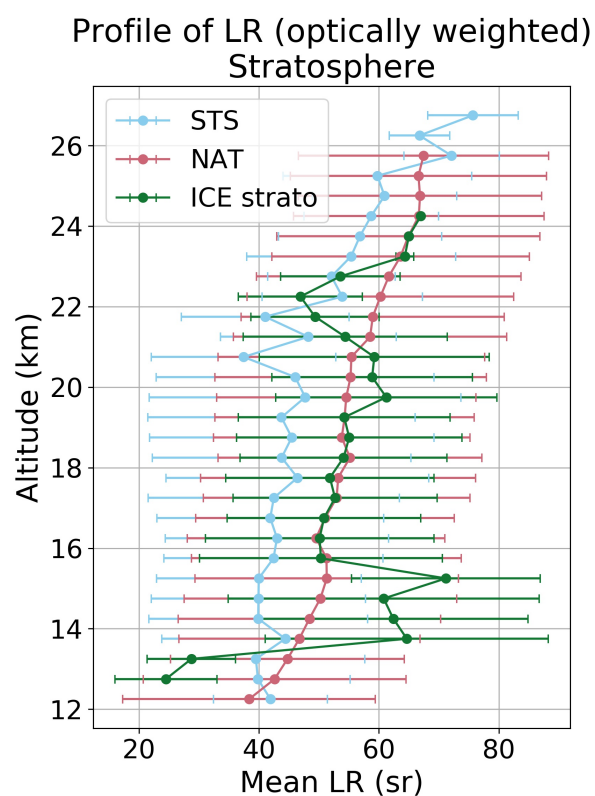


**Figure 4.** Vertical profiles of the optically-weighted median lidar ratio (thick lines) and interquartile range (shaded bars) for PSC classes (STS, NAT, ice). Only the full dataset is displayed. STS show weak vertical dependence, NAT exhibit a progressive increase in LR toward colder upper-stratospheric levels, and ice PSC display the largest variability.

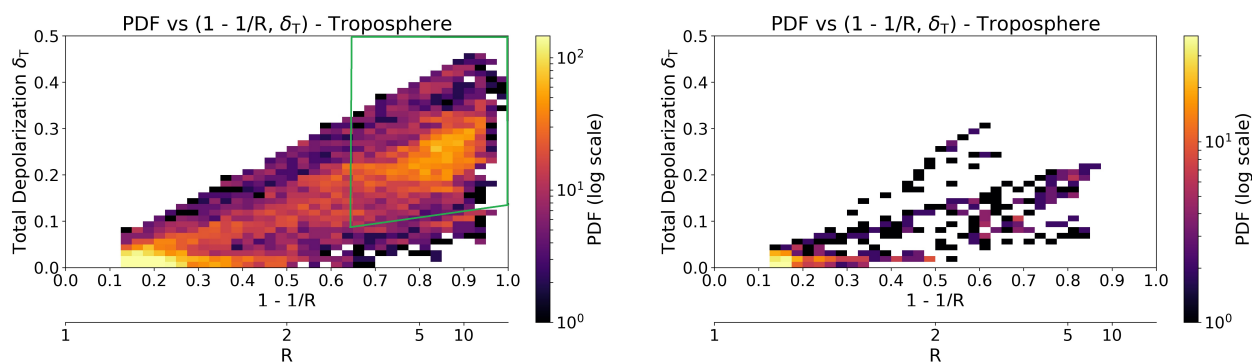


**Figure 5.** Normalized point–density PDF of tropospheric clouds in the  $(1 - 1/R), \delta_T$  phase space. Left: full dataset. Right: Young–optimized subset. Cirrus follow a continuous branch with increasing depolarization and backscatter enhancement, bounded by particle–depolarization isolines. The area bounded by green lines selects the well–developed ice clouds in the upper troposphere for further analysis. The reduced number of Young–optimized profiles mainly reflects the lower signal–to–noise ratio of the tropospheric channel rather than a microphysical selection.

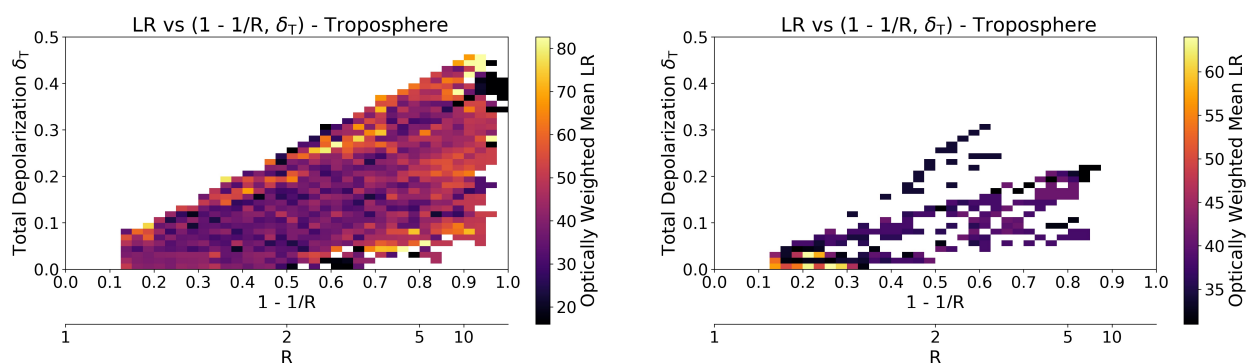


**Figure 6.** Optically–weighted mean lidar ratio (LR) for tropospheric clouds in the  $(1 - 1/R), \delta_T$  optical phase space. Left: full dataset. Right: Young–optimized subset. The full dataset spans LR  $\sim 20$ – $80$  sr with a modal region near 35–55 sr. The Young subset collapses into a narrower region (LR  $\sim 30$ – $40$  sr), reflecting the removal of clouds with noisy boundaries or strong vertical gradients while preserving the central microphysical structure of the full population.

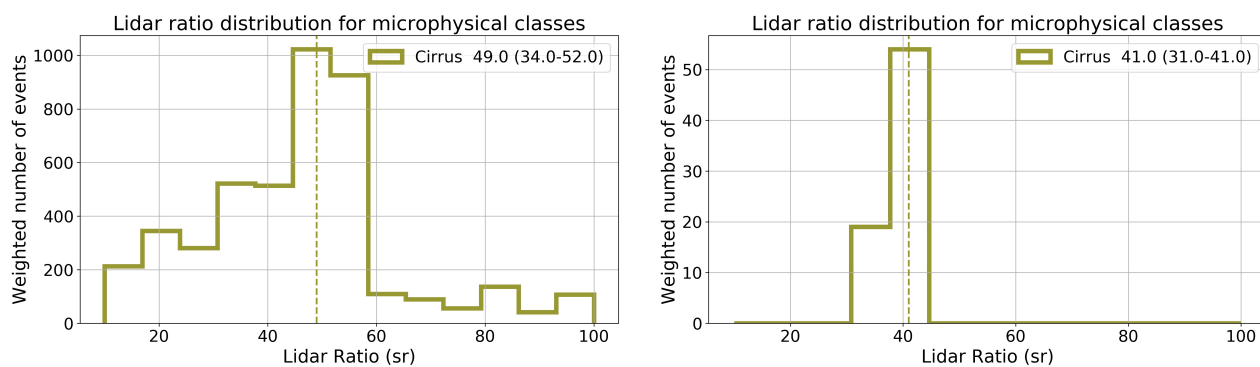


**Figure 7.** One-dimensional probability density function (PDF) of the lidar ratio (LR) for tropospheric cirrus. Left: full dataset. Right: Young-optimized subset. The full dataset exhibits a broad distribution with median  $\sim 51$  sr and a high-LR tail associated with optically thick or morphologically complex cirrus. In contrast, the Young subset converges toward a compact distribution centred at  $\sim 41$  sr, with a limited number of layers satisfying the Young optimization criteria.

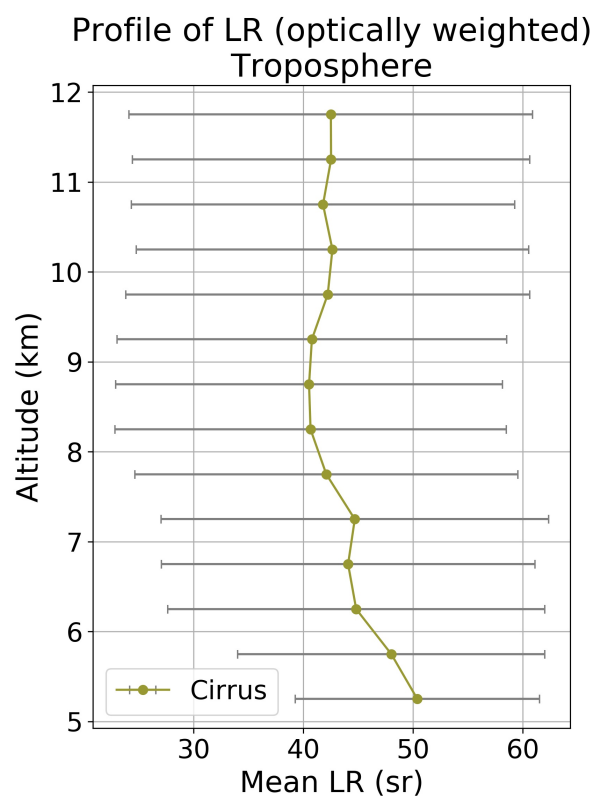


**Figure 8.** Vertical profile of optically-weighted median lidar ratio (LR) for tropospheric cirrus. Only the full dataset dataset is displayed. A weak decrease in LR with height is visible in the full dataset, consistent with smaller and less complex ice crystals near cloud top.